JOURNAL OF SPACECRAFT AND ROCKETS
Vol. 34, No. 3, May–June 1997

Internal Effects Model for Spacecraft Modules Perforated by Orbital Debris

William P. Schonberg* and John Serrano†
University of Alabama in Huntsville, Huntsville, Alabama 35899
and
Joel E. Williamsen‡
NASA Marshall Space Flight Center, Huntsville, Alabama 35812

A model is developed to predict the effect of a perforating orbital debris particle impact on the pressure and temperature within a pressurized habitable spacecraft module. The model is developed such that it sequentially characterizes the phenomena comprising the impact event, beginning with the initial impact on the outer module wall. The model then considers the creation and motion of a debris cloud within the module wall system and the impact of the debris cloud on the inner module wall. The final phase of the model is concerned with the creation and motion of the debris cloud that enters the module interior and its effect within the module on module pressure and temperature levels. This characterization is accomplished through the application of elementary shock physics theory and fundamental thermodynamic principles. The predictions of the analytical model are compared with experimental pressure and temperature data from a series of instrumented high-speed impact tests. Several modifications are made to the basic model to bring its predictions closer in line with the experimental results. Following the adjustment of several empirical constants, the predictions of the modified internal effects model are shown to be in close agreement with the experimental results.

Nomenclature

A_p = presented area of internal debris cloud, πR_{dc}^2, cm^2
C_D = internal debris cloud drag force coefficient
C_{pa} = ambient specific heat of module air, 0.24 cal/g°C
C_1, C_2 = proportionality constants
c_{0a} = ambient speed of sound in module air, 0.33 km/s
D_h = outer bumper hole diameter, cm
D_p = presented diameter of internal debris cloud, cm
D_1, D_2 = proportionality constants
d_h = inner bumper hole diameter, cm
d_p = projectile diameter, cm
E = total internal debris cloud kinetic energy; sum of axial and expansion energies, J
E_{impact} = projectile impact energy, $m_p v_0^2/2$, J
$E_{\mathrm{bmpr}}^{\mathrm{sh\&rl}}$ = bumper material residual energy per unit mass following shock heating and release, J/kg
$E_{\mathrm{debcld}}^{\mathrm{int,ax}}$ = internal debris cloud axial kinetic energy, J
$E_{\mathrm{debcld}}^{\mathrm{prim,ax}}$ = primary debris cloud axial kinetic energy, J
$E_{\mathrm{debcld}}^{\mathrm{prim,exp}}$ = primary debris cloud expansion kinetic energy, J
$E_{\mathrm{lost}}^{\mathrm{pr,ax}}$ = primary debris cloud axial kinetic energy lost due to a portion of the primary debris cloud particles being trapped by the inner bumper, J
$E_{\mathrm{lost}}^{\mathrm{pr,exp}}$ = primary debris cloud expansion kinetic energy lost due to a portion of the primary debris particles being trapped by the inner bumper, J
$E_{\mathrm{proj}}^{\mathrm{sh\&rl}}$ = projectile material residual energy per unit mass following shock heating and release, J/kg
E_0 = ambient module air energy, $C_{pa}T_0$, J
F_D = drag force on internal debris cloud due to module air, N
H = distance away from pressure wall at which shock wave attenuation begins, cm
k_a = slope of shock wave velocity-particle velocity line for air, 1.07
M = internal debris cloud Mach number, u_{sdc}/c_{0a}
m, n = positive rational numbers
m_b = bumper hole-out mass, $\pi\rho_b t_b D_h^2/4$, g
m_{ib} = inner bumper hole-out mass, $\pi\Lambda_{\mathrm{ib}} d_h^2/4$, g
m_p = projectile mass, $\pi\rho_p d_p^3/6$, g
$m_{\mathrm{debcld}}^{\mathrm{sec\ on}}$ = secondary debris cloud total mass, g
$P_a(\eta)$ = pressure at a distance η away from internal shock wave, atm
$P_s'(R')$ = nondimensional pressure as a function of R'
P_{s0}' = maximum value of nondimensional pressure
P_{0a} = ambient module air pressure, 1 atm
R' = nondimensional distance away from internal shock wave front
R_{dc} = internal debris cloud radius at onset of attenuation, cm
T_0 = ambient module air temperature, 297 K
t_b = bumper thickness, cm
t_w = pressure wall thickness, cm
u_{exp} = internal debris cloud expansion velocity, km/s
u_{mc} = internal debris cloud axial velocity, km/s
u_{sdc} = speed of shock wave in module air, km/s
V = generic debris cloud motion velocity, km/s
$v_{\mathrm{exp}}^{\mathrm{prim}}$ = primary debris cloud expansion velocity, km/s
$v_{\mathrm{exp}}^{\mathrm{sec}}$ = secondary debris cloud average expansion velocity, km/s
$v_{\mathrm{exp}}^{\mathrm{sec\ 1}}$ = secondary debris cloud first component expansion velocity, km/s
$v_{\mathrm{exp}}^{\mathrm{sec\ 2}}$ = secondary debris cloud second component expansion velocity, km/s
$v_{\mathrm{mc}}^{\mathrm{prim}}$ = primary debris cloud axial velocity, km/s
$v_{\mathrm{mc}}^{\mathrm{sec}}$ = secondary debris cloud average axial velocity, km/s
$v_{\mathrm{mc}}^{\mathrm{sec\ 1}}$ = secondary debris cloud first component axial velocity, km/s
$v_{\mathrm{mc}}^{\mathrm{sec\ 2}}$ = secondary debris cloud second component axial velocity, km/s
v_0 = projectile impact velocity, km/s
x_{poi} = point of interest x coordinate, cm
$\theta_{\mathrm{dc}}^{\mathrm{prim}}$ = semicone angle defining primary debris cloud spread, deg or rad

Received July 11, 1996; revision received Dec. 9, 1996; accepted for publication Dec. 10, 1996.

*Professor, Civil and Environmental Engineering Department. Senior Member AIAA.
†Senior Ballistics Specialist, Aerophysics Research Center.
‡Aerospace Engineer, Structural Development Branch, Mail Code ED-52. Member AIAA.

$\theta_{dc}^{sec\ 1}$ = semicone angle defining secondary debris cloud first component spread, deg or rad
$\theta_{dc}^{sec\ 2}$ = semicone angle defining secondary debris cloud second component spread, deg or rad
κ_1 = primary debris cloud mass reduction factor
κ_2 = empirical constant that controls the rate of shock wave attenuation
Λ_{ib} = inner bumper areal mass density, g/cm^2
Λ_{pw} = pressure wall areal mass density, $\rho_w t_w$, g/cm^2
μ_a = ambient viscosity of module air, 1.78×10^{-5} kg/m-s
ρ_b = bumper material mass density, g/cm^3
ρ_p = projectile material mass density, g/cm^3
ρ_w = pressure wall material mass density, g/cm^3
ρ_{0a} = ambient density of module air, 1.22×10^{-3} g/cm^3

Introduction

A FIRST-PRINCIPLES-based model is developed to predict the internal effects within a pressurized spacecraft module following a perforating orbital debris particle impact. Although the effects of a perforating debris particle on crew and equipment can be severe, only a limited number of empirical internal effects studies focusing on space vehicles have been performed to date.[1–3] Traditionally, crew loss or incapacitation due to a perforating impact has primarily been of interest to military organizations and as such have focused on military vehicles and systems.[4] The internal effects considered in this study are the rise in ambient pressure and temperature within a habitable spacecraft module. The module has as its wall a standard Whipple-type dual-wall system (see Fig. 1) in which the outer wall (or bumper) protects the module and its inhabitants by disrupting impacting particles.

Following the high-speed impact of a projectile on the outer bumper of the system shown in Fig. 1, shock waves are set up in the projectile and bumper materials. The pressures associated with these shocks typically exceed the strengths of the materials by several orders of magnitude. For example, in an 8-km/s aluminum-on-aluminum impact, the ratio of the impact pressure (116.5 GPa = 1.15 Mbar) to the strength of the material (310 MPa for aluminum 6061-T6) is approximately 375, or roughly 2.5 orders of magnitude. As the shock waves propagate, the projectile and bumper materials are heated adiabatically and nonisentropically. The release of the shock pressures occurs isentropically through the action of rarefaction waves that are generated as the shock waves interact with the free surfaces of the projectile and bumper. This process can cause either or both materials to fragment, melt, or vaporize, depending on the material properties, geometric parameters, and the velocity of impact.

In this manner, a debris cloud consisting of fragmented, melted, or vaporized projectile and bumper material (referred to hereafter as the primary debris cloud) is created. This debris cloud travels toward, impacts, and perforates the inner bumper. For this study, the inner bumper consists of either a blanket of multilayer thermal insulation (MLI) or a multimaterial composite wall (type A and type B inner bumpers, respectively). In addition to providing thermal insulation, the inner bumper serves to trap some or most of the primary debris cloud particles. The debris cloud exiting the inner bumper is referred to as the secondary debris cloud.

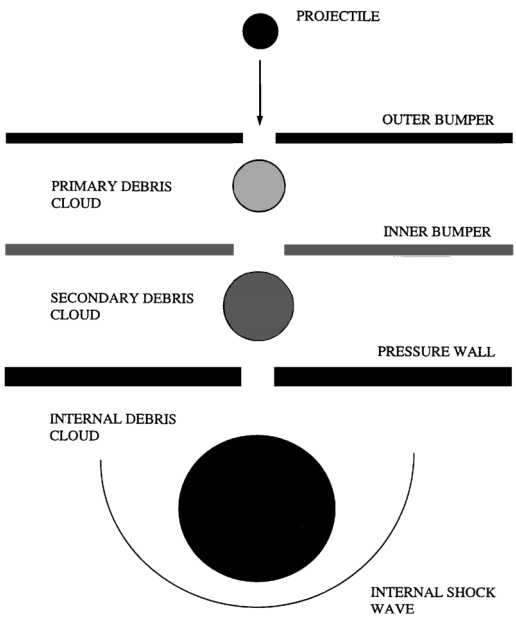

Fig. 1 Hypervelocity impact of a generic multiwall structure.

Eventually, the secondary debris cloud impacts the inner or pressure wall of the multiwall system. The material in the secondary debris cloud and the portion of the pressure wall impacted by the secondary debris cloud are shocked and released in a manner similar to that of the projectile and outer bumper material. In some instances, this causes a perforation of the pressure wall. If this were to occur in an orbiting habitable module, then the debris cloud created as a result of the pressure wall perforation (hereafter referred to as the internal debris cloud) would be ejected into the module interior. In addition to the motion of the internal debris cloud within the module, a shock wave would also be created in the module due to the presence of the module air. As a result, there exists a concern regarding the effect of the passage of the internal debris cloud and the shock wave it generates on ambient module pressures and temperatures.

In an attempt to address this issue, an analytical model is developed to characterize the motion of the internal debris cloud within the module and its effects on pressure and temperature within a pressurized habitable module. The model is developed such that it sequentially characterizes the phenomena composing the impact event, including the initial impact on the outer module wall, the creation and motion of a debris cloud within the module-wall system, the impact of the debris cloud on the inner module wall, the creation and motion of the debris cloud that enters the module interior, and the effects of the debris cloud within the module on module pressure and temperature levels. This characterization is accomplished through the application of elementary shock physics theory and fundamental thermodynamic principles. Following the development of the analytical model, its predictions are compared with experimental pressure and temperature data from a series of instrumented high-speed impact tests. Modifications to the model that are required to bring its predictions in closer agreement with the experimental results are then presented and discussed.

Initial Impact Shock Loading and Release Modeling

In calculating the shock loading and subsequent release of the projectile and bumper materials, the shock waves are considered to be initially planar. This simplification allows one-dimensional relationships to be used for analyzing the creation and release of shock pressures. In this manner, the shock pressures, energies, etc., in the projectile and bumper materials are calculated using the three one-dimensional shock-jump conditions, a linear relationship between the shock wave velocity and particle velocity in each material, and continuity of pressure and velocity at the projectile/target interface. This process completely defines the shocked states of the projectile and target materials due to the initial impact.

Whereas the shock loading of a material is an irreversible process that results in an increase of the internal energy of the shocked material, the release of a shocked material occurs isentropically along a release adiabat. To calculate the release of the projectile and target materials from their respective shocked states, an appropriate equation of state is needed for each material. To keep the analysis relatively simple, the Mie–Gruneisen equation of state[5] was used in this study.

The Mie–Gruneisen equation of state (EOS) is an accurate thermodynamic description of most metals in the solid regime and is relatively easy to use. Invoking the second law of thermodynamics allows us to construct the release isentrope in pressure-volume space for a material referenced to the material Hugoniot and a given initial shocked state.[5] Although the Mie–Gruneisen EOS cannot be expected to give accurate results in a highly expanded liquid regime or in a vapor regime, experience has shown that it does yield fairly accurate end-state results even when there is a small percentage of molten material present.[6]

Modeling of Primary and Secondary Debris Clouds

Primary Debris Cloud Mass

The mass of the primary debris cloud consists of the mass of the original impacting projectile plus the mass of the removed bumper material. No mass is considered lost to backsplash of the bumper and projectile materials; hence, because all of the mass is presumed to be directed in toward the pressure wall, the model to be developed should yield conservative results. The contribution of the bumper material to the primary debris cloud mass can be determined once the bumper hole diameter is known. This diameter can be calculated using any one of a number of empirical equations for hole diameter in a thin plate due to a high-speed impact.[7]

Primary Debris Cloud Characteristic Velocities

The characteristic velocities of interest for the primary debris cloud are the axial and expansion velocities. These values are determined by an application of momentum and energy conservation as follows. Because the initial impact occurs at such a high velocity, momentum transfer to the bumper itself can be ignored. As a result, using momentum conservation to calculate the axial velocity of the primary debris cloud $v_{\mathrm{mc}}^{\mathrm{prim}}$ yields the following result:

$$v_{\mathrm{mc}}^{\mathrm{prim}} = \frac{m_p v_0}{m_p + m_b} \tag{1}$$

Because of the rapidity of the impact event, the only significant energy losses are to the accompanying light flash and the shock heating of the bumper and projectile materials. If we neglect the energy associated with the light flash, then the following energy balance can be written before and after the initial impact:

$$E_{\mathrm{impact}} = E_{\mathrm{proj}}^{\mathrm{sh\&rl}} m_p + E_{\mathrm{bmpr}}^{\mathrm{sh\&rl}} m_b + E_{\mathrm{debcld}}^{\mathrm{prim,ax}} + E_{\mathrm{debcld}}^{\mathrm{prim,exp}} \tag{2}$$

If we let $v_{\mathrm{exp}}^{\mathrm{prim}}$ denote the expansion velocity of the primary debris cloud, then we can write

$$E_{\mathrm{debcld}}^{\mathrm{prim,exp}} = \frac{(m_p + m_b)\left(v_{\mathrm{exp}}^{\mathrm{prim}}\right)^2}{2} \tag{3a}$$

$$E_{\mathrm{debcld}}^{\mathrm{prim,ax}} = \frac{(m_p + m_b)\left(v_{\mathrm{mc}}^{\mathrm{prim}}\right)^2}{2} \tag{3b}$$

Substituting Eqs. (3a) and (3b) into Eq. (2) and solving for $v_{\mathrm{exp}}^{\mathrm{prim}}$ yields

$$v_{\mathrm{exp}}^{\mathrm{prim}} = \sqrt{\frac{m_p v_0^2/2 - \left[E_{\mathrm{proj}}^{\mathrm{sh\&rl}} m_p + E_{\mathrm{bmpr}}^{\mathrm{sh\&rl}} m_b + (m_p + m_b)\left(v_{\mathrm{mc}}^{\mathrm{prim}}\right)^2/2\right]}{(m_p + m_b)/2}} \tag{4}$$

Finally, note that the spread of the primary debris cloud (in this case the half-angle defining the spread) can be estimated using the following relationship between the calculated primary debris cloud expansion and axial velocities:

$$\theta_{\mathrm{dc}}^{\mathrm{prim}} = \tan^{-1}\left(\frac{v_{\mathrm{exp}}^{\mathrm{prim}}}{v_{\mathrm{mc}}^{\mathrm{prim}}}\right) \tag{5}$$

Secondary Debris Cloud Mass

The mass of the secondary debris cloud consists of a portion of the primary debris cloud mass plus the mass of the removed inner bumper material. Again, no mass is considered lost to backsplash of the inner bumper and primary debris cloud material. However, the fraction of primary debris cloud particles trapped by the inner bumper can be significant, especially for type B inner bumpers. The reduction in mass of the primary debris cloud as it transforms into the secondary debris cloud is obtained using a simple multiplicative reduction factor, denoted by κ_1.

From a review of the experimental test results used to verify the model being developed, it is apparent that a type A inner wall traps only a small amount of the primary debris cloud material, whereas type B traps a more significant quantity of material. One of the most distinguishing differences between the two inner bumper types (and a direct consequence of their respective composition) is their areal densities: $0.072\,\mathrm{g/cm^2}$ for the type A inner bumper and $1.17\,\mathrm{g/cm^2}$ for the type B inner bumper. Thus, it appears that the trapping capability of the inner bumpers is directly related to their areal densities. The following expression for κ_1 captures this feature:

$$\kappa_1 = \left(1 - \frac{\Lambda_{\mathrm{ib}}}{\Lambda_w}\right)^n \tag{6}$$

The contribution of the inner bumper material to the secondary debris cloud mass can be determined once the inner bumper hole diameter is known. This diameter is calculated using an empirical equation for hole diameter in a thin plate due to a high-speed impact.[8] Thus, the total mass of the secondary debris cloud can be written as

$$m_{\mathrm{debcld}}^{\mathrm{sec\ on}} = \kappa_1(m_p + m_b) + \pi \Lambda_{\mathrm{ib}} d_h^2/4 \tag{7}$$

The component of the secondary debris cloud whose origin can be traced back to the primary debris cloud is hereafter referred to as the first component, whereas the inner bumper contribution to the secondary debris cloud is hereafter referred to as the second component.

Secondary Debris Cloud Characteristic Velocities

As in the case of the primary debris cloud, the characteristic velocities of interest for the secondary debris cloud are the axial and expansion velocities. These values can be determined in a manner analogous to the procedure just presented for the primary debris cloud. However, there is a significant difference between the method developed herein for the secondary debris cloud and that for the primary debris cloud. This difference stems from the difference in the way the material is distributed within the two debris clouds.

For the purposes of this model, the primary debris cloud was tacitly assumed to be homogeneous and spherical; although it could possibly contain two different materials, both the projectile and bumper material that composed the primary debris cloud were presumed to be evenly distributed throughout the cloud. As a result, only one axial velocity and one radial velocity were required to characterize its motion and expansion, respectively. However, the secondary debris cloud comprises two very distinct material types: the more dense primary debris cloud material that passes through the inner bumper (i.e., the first component) and the less dense inner bumper material itself (i.e., the second component), which is typically some form of composite material. Thus, it is necessary to develop axial and radial velocities for each component of the secondary debris cloud.

The procedures for calculating the axial and expansion velocities are, in fact, very similar to those used for the primary debris cloud. In both cases, we first determine an average velocity quantity of interest (i.e., the average axial motion velocity or the average expansion velocity for the entire secondary debris cloud). In the case of the axial velocity, this is done by conserving momentum before and after the impact of the primary debris cloud on the inner bumper; for the expansion velocity, this is done using energy conservation before and after the inner bumper impact. Next, we postulate that the two velocity quantities of interest for both components are proportional to the average velocity quantity just calculated. Finally, we solve for the proportionality constants by conserving appropriate momentum and energy quantities.

In this manner, for the axial velocities of the two components of the secondary debris cloud, we write

$$v_{\mathrm{mc}}^{\mathrm{sec\ 1}} = C_1 v_{\mathrm{mc}}^{\mathrm{sec}} \tag{8a}$$

$$v_{\mathrm{mc}}^{\mathrm{sec\ 2}} = C_2 v_{\mathrm{mc}}^{\mathrm{sec}} \tag{8b}$$

where the proportionality constants C_1 and C_2 have to be determined and

$$v_{\mathrm{mc}}^{\mathrm{sec}} = \frac{(m_p + m_b)v_{\mathrm{mc}}^{\mathrm{prim}}}{m_{\mathrm{debcld}}^{\mathrm{sec\,on}}} \tag{9}$$

Momentum conservation before and after the impact of the primary debris cloud on the inner bumper yields

$$(m_p + m_b)v_{\mathrm{mc}}^{\mathrm{prim}} = \kappa_1(m_p + m_b)v_{\mathrm{mc}}^{\mathrm{sec\,1}} + m_{\mathrm{ib}}v_{\mathrm{mc}}^{\mathrm{sec\,2}} \tag{10}$$

Substituting Eqs. (8a) and (8b) into Eq. (10) and rearranging yields

$$\kappa_1(m_p + m_b)C_1 + m_{\mathrm{ib}}C_2 = (m_p + m_b)\left(\frac{v_{\mathrm{mc}}^{\mathrm{prim}}}{v_{\mathrm{mc}}^{\mathrm{sec}}}\right) \tag{11a}$$

A second equation for C_1 and C_2 is obtained by conserving the kinetic energy associated with the axial motion of the primary and secondary debris clouds. This equation is written as follows:

$$\frac{(m_p + m_b)\left(v_{\mathrm{mc}}^{\mathrm{prim}}\right)^2}{2} = \frac{\kappa_1(m_p + m_b)\left(v_{\mathrm{mc}}^{\mathrm{sec\,1}}\right)^2}{2} + \frac{m_{\mathrm{ib}}\left(v_{\mathrm{mc}}^{\mathrm{sec\,2}}\right)^2}{2} + E_{\mathrm{lost}}^{\mathrm{pr,ax}} \tag{11b}$$

The energy loss in Eq. (11b) is written as

$$E_{\mathrm{lost}}^{\mathrm{pr,ax}} = \frac{(1 - \kappa_1)(m_p + m_b)\left(v_{\mathrm{mc}}^{\mathrm{prim}}\right)^2}{2} \tag{12}$$

Substituting Eqs. (8a), (8b), and (12) into Eq. (11b) and rearranging yields

$$\kappa_1(m_p + m_b)C_1^2 + m_{\mathrm{ib}}C_2^2 = \kappa_1(m_p + m_b)\left(\frac{v_{\mathrm{mc}}^{\mathrm{prim}}}{v_{\mathrm{mc}}^{\mathrm{sec}}}\right)^2 \tag{13}$$

Solving Eqs. (11a) and (13) yields

$$C_1 = \frac{\xi_a - \beta C_2}{\alpha} \tag{14a}$$

$$C_2 = \xi_a \frac{(\beta/\alpha) - \sqrt{\Delta}}{\beta[(\beta/\alpha) + 1]} \tag{14b}$$

where

$$\Delta = (\beta/\alpha)\left\{[(\beta/\alpha) + 1]\kappa_1^2 - 1\right\} \tag{15a}$$

and where

$$\alpha = \kappa_1(m_p + m_b) \tag{15b}$$

$$\beta = m_{\mathrm{ib}} \tag{15c}$$

$$\xi_a = (m_p + m_b)\left(\frac{v_{\mathrm{mc}}^{\mathrm{prim}}}{v_{\mathrm{mc}}^{\mathrm{sec}}}\right) \tag{15d}$$

Similarly, to obtain the expression for the expansion velocities of the two secondary debris cloud components, we begin by writing

$$v_{\mathrm{exp}}^{\mathrm{sec\,1}} = D_1 v_{\mathrm{exp}}^{\mathrm{sec}} \tag{16a}$$

$$v_{\mathrm{exp}}^{\mathrm{sec\,2}} = D_2 v_{\mathrm{exp}}^{\mathrm{sec}} \tag{16b}$$

where

$$v_{\mathrm{exp}}^{\mathrm{sec}} = \frac{\sqrt{\kappa_1\left[(m_p + m_b)\left(v_{\mathrm{mc}}^{\mathrm{prim}}\right)^2 + (m_p + m_b)\left(v_{\mathrm{exp}}^{\mathrm{prim}}\right)^2\right] - m_{\mathrm{debcld}}^{\mathrm{sec\,on}}\left(v_{\mathrm{mc}}^{\mathrm{sec}}\right)^2}}{m_{\mathrm{debcld}}^{\mathrm{sec\,on}}} \tag{17}$$

Next, we conserve the kinetic energy associated with the expansion of the two secondary debris cloud components

$$\frac{(m_p + m_b)\left(v_{\mathrm{exp}}^{\mathrm{prim}}\right)^2}{2} = \frac{\kappa_1(m_p + m_b)\left(v_{\mathrm{exp}}^{\mathrm{sec\,1}}\right)^2}{2} + \frac{m_{\mathrm{ib}}\left(v_{\mathrm{exp}}^{\mathrm{sec\,2}}\right)^2}{2} + E_{\mathrm{lost}}^{\mathrm{pr,exp}} \tag{18}$$

The energy loss in Eq. (18) is written as

$$E_{\mathrm{lost}}^{\mathrm{pr,exp}} = \frac{(1 - \kappa_1)(m_p + m_b)\left(v_{\mathrm{exp}}^{\mathrm{prim}}\right)^2}{2} \tag{19}$$

Substituting Eqs. (16a), (16b), and (19) into Eq. (18) yields

$$\kappa_1(m_p + m_b)D_1^2 + m_{\mathrm{ib}}D_2^2 = \kappa_1(m_p + m_b)\left(\frac{v_{\mathrm{exp}}^{\mathrm{prim}}}{v_{\mathrm{exp}}^{\mathrm{sec}}}\right)^2 \tag{20}$$

A second equation for D_1 and D_2 is obtained by conserving the momentum associated with the expansion of the primary and secondary debris clouds:

$$(m_p + m_b)v_{\mathrm{exp}}^{\mathrm{prim}} = \kappa_1(m_p + m_b)v_{\mathrm{exp}}^{\mathrm{sec\,1}} + m_{\mathrm{ib}}v_{\mathrm{exp}}^{\mathrm{sec\,2}} \tag{21}$$

Substituting Eqs. (16a) and (16b) into Eq. (21) yields

$$\kappa_1(m_p + m_b)D_1 + m_{\mathrm{ib}}D_2 = (m_p + m_b)\left(\frac{v_{\mathrm{exp}}^{\mathrm{prim}}}{v_{\mathrm{exp}}^{\mathrm{sec}}}\right) \tag{22}$$

Thus, the constants D_1 and D_2 are found by solving Eqs. (20) and (22). However, if we compare Eqs. (20) and (22) to Eqs. (11a) and (13), we find them to be identical with the exception that Eqs. (20) and (22) are written in terms of expansion velocities whereas Eqs. (11a) and (13) are in terms of axial motion velocities. Other than that difference, their basic forms are identical. Therefore, the solution for the constants D_1 and D_2 is written directly from Eqs. (14) and (15) as follows:

$$D_1 = \frac{\xi_e - \beta D_2}{\alpha} \tag{23a}$$

$$D_2 = \frac{\xi_e[(\beta/\alpha) - \sqrt{\Delta}]}{\beta[(\beta/\alpha) + 1]} \tag{23b}$$

where

$$\xi_e = (m_p + m_b)\left(\frac{v_{\mathrm{exp}}^{\mathrm{prim}}}{v_{\mathrm{exp}}^{\mathrm{sec}}}\right) \tag{24}$$

and where Δ, α, and β are given by Eqs. (15a), (15b), and (15c), respectively.

As before, the spread angles of the two secondary debris cloud components (in this case the half-angles defining the spreads) can be estimated using the following relationships between the calculated secondary debris cloud expansion and axial velocities:

$$\theta_{\mathrm{dc}}^{\mathrm{sec\,1}} = \tan^{-1}\left(\frac{v_{\mathrm{exp}}^{\mathrm{sec\,1}}}{v_{\mathrm{mc}}^{\mathrm{sec\,1}}}\right) \tag{25a}$$

$$\theta_{\mathrm{dc}}^{\mathrm{sec\,2}} = \tan^{-1}\left(\frac{v_{\mathrm{exp}}^{\mathrm{sec\,2}}}{v_{\mathrm{mc}}^{\mathrm{sec\,2}}}\right) \tag{25b}$$

Pressure Wall Impact Shock Loading and Release Modeling

In modeling the shock loading and subsequent release of the secondary debris cloud and pressure wall materials, it is again presumed that the shock waves in the pressure wall are initially planar, which again allows one-dimensional relationships to be used for analyzing the creation and release of shock pressures. The process used to calculate shock pressures, energies, etc., in the debris cloud and pressure wall materials is nearly identical to that used in modeling

the initial impact of the projectile on the bumper, with the following exceptions. First, only the secondary debris cloud material component consisting of primary debris cloud material that passed through the inner bumper is assumed to contribute to the impact loading of the pressure wall. As such, the properties of that component of the secondary debris cloud and pressure wall properties are used in place of projectile and bumper properties, respectively. The component of the secondary debris cloud consisting of inner bumper material contributes only to the impulsive loading of the pressure wall. Whereas this load is significant for impacts that do not perforate the module pressure wall, its effects are minimal when compared against perforating load magnitudes. Second, the initial density of the secondary debris cloud material considered in the impact analysis is taken as the average of the final densities after release from their respective shocked states of the projectile and bumper materials in the primary debris cloud. Finally, the secondary debris cloud axial velocity given by Eq. (9) is used as the impact velocity in the analysis.

Effect of Internal Debris Cloud Passage

Debris Cloud Induced Pressure and Temperature Changes

In the event that module wall perforation results in a debris cloud entering the module interior, the temperature rise and pressure increase accompanying the passage of a shock wave created by the motion of such a debris cloud are determined as follows. First, the speed of the shock wave created by the motion of the internal debris cloud through the module air (subsequently referred to as u_{sdc}) is taken to be equal to the leading-edge velocity of the debris cloud, which can be approximated by the particle velocity at the pressure wall/module air interface. This velocity quantity is found using a technique based on the method of impedance matching[9] in which continuity of pressure and particle velocity are enforced at the pressure wall/module air interface. Although this may be presumed to be only valid in the immediate vicinity of the leading edge of the debris cloud near its centerline, applying this equality to the entire shock wave generated by the debris cloud should yield conservative results.

Second, it is further assumed that the speed of the debris cloud and its accompanying shock wave do not decay until they are at a certain distance away from the perforated pressure wall. If this distance is less than a module diameter, then the debris cloud effectively runs out of steam at this location and the velocity drops quickly to zero. It is at this distance (and point in time) that the attenuation of the shock wave induced pressures and temperatures begin. This assumption allows us to treat the shock wave velocity as essentially constant, which is consistent with the conservative nature of the model being developed. The method for calculating the distance at which attenuation begins is presented in a subsequent section.

Figure 2 shows a sketch of a generic debris cloud moving through the interior of a module and the shock wave accompanying its motion. Following the definition of the shock wave velocity u_{sdc} employed herein, the particle velocity in the air induced by the shock wave is given by

$$u_{pdc} = \frac{u_{sdc} - c_{0a}}{k_a} \tag{26}$$

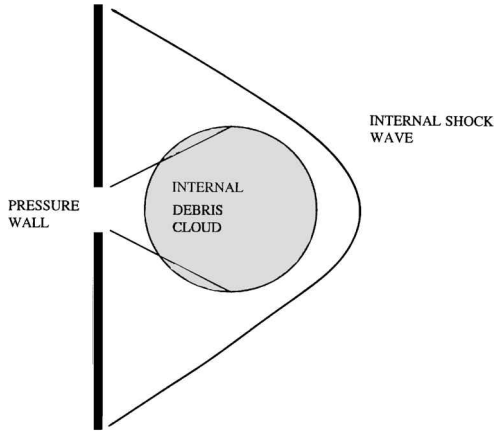

Fig. 2 Internal debris cloud with accompanying shock wave.

In this manner, the pressure behind the shock is given by

$$P_{Ha} = P_{0a} + \rho_{0a} u_{sdc} u_{pdc} \tag{27}$$

The shocked density is given by

$$\rho_{Ha} = \frac{u_{sdc}\rho_{0a}}{u_{sdc} - u_{pdc}} \tag{28}$$

Prior to the decay of the shock wave, the temperature increase in the immediate vicinity of the pressure wall is given by

$$\Delta T = \frac{E_{Ha} - E_{0a}}{C_{pa}} \tag{29}$$

where E_{Ha} is given by

$$E_{Ha} = E_{0a} + \tfrac{1}{2}(P_{Ha} + P_{0a})(1/\rho_{0a} - 1/\rho_{Ha}) \tag{30}$$

Thus, ΔT and $\Delta P = P_{Ha} - P_{0a}$ define the change in pressure and temperature due to an internal debris cloud traveling within a pressurized module in the immediate vicinity of the debris cloud itself.

Attenuation of Debris Cloud Induced Pressures

As the debris cloud moves through the module interior, it continuously sets up a shock wave in the module air. Thus, attenuation of the shock wave so created can occur only when there is no longer any debris cloud motion. In keeping with the assumption of constant debris cloud velocity, it is presumed that debris cloud motion ceases either when the debris cloud impacts an obstacle such as the far module wall or when the drag force due to the presence of air within the module exhausts the axial kinetic energy of the debris cloud, whichever comes first. It is at this instant that the attenuation of the shock wave is begun.

Figure 3 shows a sketch of this scenario and the geometric parameters required to perform this calculation. The decay with distance of the initial pressure and temperature induced by the shock wave in the module is obtained using the nondimensional attenuation data for spherical air blast waves.[10] The initial pressure P_{Ha} is attenuated as function of distance η away from the origination point of the shock wave by scaling the nondimensional values of pressure and distance in Ref. 10 to P_{Ha} and η, respectively, beginning with the maximum value of the nondimensional pressure. In this manner, we have

$$P_a(\eta) = \frac{P_s'(R')}{P_{s0}'} P_{Ha} \tag{31}$$

The dimensional distance η is obtained from its nondimensional counterpart R' using the relationship[10]

$$\eta = R'(E/P_{0a})^{\frac{1}{3}} \tag{32}$$

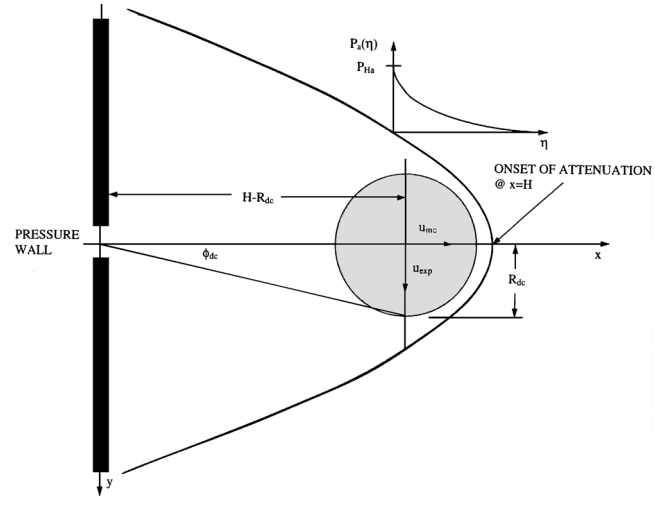

Fig. 3 Onset of internal debris cloud shock wave attenuation.

The kinetic energy of the internal debris cloud is calculated by performing a momentum and energy balance before and after the impact of the secondary debris cloud on the pressure wall.

To find temperature decay with distance η, we use the following slightly modified forms of Eqs. (29) and (30):

$$\Delta T = \frac{E_a(\eta) - E_{0a}}{C_{pa}} \tag{33}$$

where $P_a(\eta)$ is given by Eq. (31),

$$E_a(\eta) = E_{0a} + \frac{1}{2}[P_a(\eta) + P_{0a}]\left[\frac{1}{\rho_{0a}} - \frac{1}{\rho_a(\eta)}\right] \tag{34}$$

is the energy behind a decaying shock wave as a function of the distance η, and $\rho_a(\eta)$ is the corresponding shocked air density. In this case, the density of the air behind a decaying shock wave is given as a function of η by the following modified form of Eq. (28):

$$\rho_a(\eta) = \frac{u_s(\eta)\rho_{0a}}{u_s(\eta) - u_p(\eta)} \tag{35}$$

where

$$u_s(\eta) = c_{0a} + k_a u_p(\eta) \tag{36}$$

is the speed of the decaying shock wave as a function of η and $u_p(\eta)$ is the corresponding particle velocity (also a function of the distance η). Finally, the particle velocity as a function of distance is found by substituting Eq. (36) into the following alternate expression for $P_a(\eta)$:

$$P_a(\eta) = P_{0a} + \rho_{0a} u_s(\eta) u_p(\eta) \tag{37}$$

Solving for $u_p(\eta)$ thus yields

$$u_p(\eta) = \frac{-\rho_{0a}c_{0a} + \sqrt{\Delta}}{2k_a\rho_{0a}} \tag{38}$$

where

$$\Delta = (\rho_{0a}c_{0a})^2 - 4k_a\rho_{0a}[P_{0a} - P_a(\eta)] \tag{39}$$

Onset of Pressure and Temperature Attenuation

Referring to Fig. 3, the distance away from the pressure wall at which the attenuation of the shock wave induced pressures and temperatures begins is denoted by H. This distance is calculated by balancing the axial kinetic energy of the debris cloud and the work done by the drag force due to the presence of the module air as the debris cloud moves through the module. Thus, we write

$$E^{\text{int,ax}}_{\text{debcld}} = F_D H \tag{40}$$

Elementary fluid dynamics provides the following expression to calculate the drag force:

$$F_D = \frac{\rho_a C_D A_p V^2}{2} \tag{41}$$

The drag coefficient C_D is typically a function of the Reynolds number Re, which itself is given by

$$Re = \frac{\rho_a V D_p}{\mu_a} \tag{42}$$

Assuming a nominal presented diameter $D_p = 10$ cm and a nominal motion velocity $V = 1$ km/s and substituting these values into Eq. (42) yields a Reynolds number in excess of 10^6. In this Reynolds number regime, the drag coefficient curve for a sphere is relatively flat with a value between 0.1 and 0.3. The specific value of C_D used in this model will be discussed in a later section.

To solve for the distance H, we note that the radius of the debris cloud at the onset of attenuation can be obtained using the following relationships between debris cloud spread half-angle, the axial and transverse debris cloud velocities, and the geometry involved:

$$\sin\phi_{\text{dc}} = \frac{R_{\text{dc}}}{H - R_{\text{dc}}} \tag{43a}$$

$$\phi_{\text{dc}} = \tan^{-1}(u_{\text{exp}}/u_{\text{mc}}) \tag{43b}$$

As before, the axial and expansion velocities of the internal debris cloud are obtained by conserving momentum and energy before and after the impact of the first secondary debris cloud component on the pressure wall. Thus, we have

$$R_{\text{dc}} = H f_\phi \tag{44a}$$

$$f_\phi = \frac{\sin\phi_{\text{dc}}}{1 + \sin\phi_{\text{dc}}} \tag{44b}$$

Substituting Eqs. (41) and (44b) into Eq. (40), we obtain

$$E^{\text{int,ax}}_{\text{debcld}} = \frac{\pi C_D \rho_a f_\phi^2 u_{\text{mc}}^2 H^3}{2} \tag{45}$$

where V has been replaced by u_{mc}. Solving for H yields

$$H = \sqrt[3]{\frac{E^{\text{int,ax}}_{\text{debcld}}}{\pi C_D \rho_a f_\phi^2 u_{\text{mc}}^2 / 2}} \tag{46}$$

Pressure and Temperature Values at a Specified Location

To determine the pressure and temperature values at a specified location within the module due to the passage of the internal debris cloud, several preliminary issues must be addressed. These issues are discussed sequentially and are followed by a development of the equations required to obtain the desired information. First, if the point of interest is within the cone angle formed the motion and expansion of the internal debris cloud (region ABC in Fig. 4), then personnel at the point of interest will probably be struck by the debris cloud itself. Second, if the point of interest is not within the cone angle characterizing the spread of the debris cloud but is within the volume of air that is traversed by the shock wave induced by the motion of the debris cloud (region CAD in Fig. 4), then personnel at the point of interest will feel the full pressure and temperature associated with the passage of the shock wave itself. Hence, it is not necessary to perform any attenuation of the shock wave induced pressure and temperature increases for such points of interest. Third, although the shock wave is presumed not to fan out during decay, its growth in the lateral direction (i.e., perpendicular to the axial

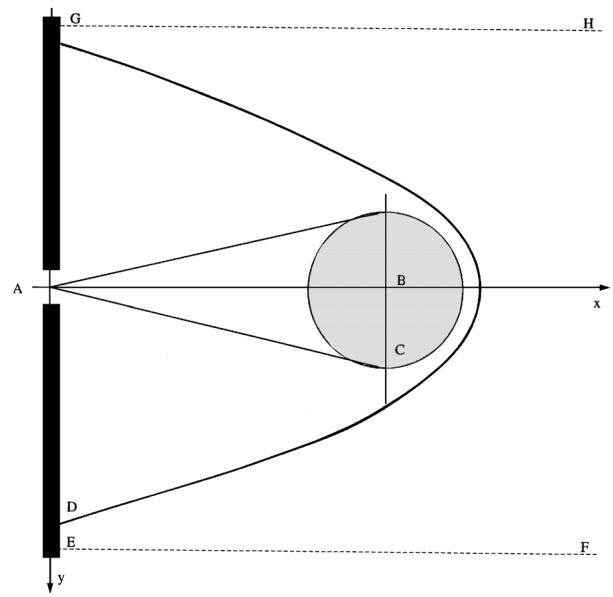

Fig. 4 Pressure and temperature values at a specific location.

direction of its motion) can still be observed, as shown in Fig. 4. If the point of interest is outside region HGEF, i.e., the cylindrical volume of module air whose base corresponds to the maximum extent of the attenuating shock wave, then personnel at the point of interest will not feel any of the effects of the debris cloud shock wave. Fourth, once the pressure jump across the decaying shock wave (i.e., in the x direction) is less than 1% of ambient, it is assumed that we are, in fact, at ambient conditions and the attenuation process stops. Any point of interest that lies ahead of the shock wave in such a state will not experience any of the effects of the debris cloud or the shock wave it creates, whereas a point of interest behind it will. Naturally, the attenuation process must first be performed to identify the position of this decayed shock wave, after which it can then be determined whether or not the point of interest lies behind it or ahead of it. If during the attenuation process the point of interest is traversed by the decaying shock wave, then the attenuation process stops and the pressure and temperature at the point of interest are available.

Definition of Shock Wave Position

Based on the discussion in the preceding section, it is apparent that a functional form of the shock wave at the time attenuation begins and throughout the attenuation process is required. We begin by considering a shock wave in two dimensions and then extend the results to three dimensions. The equation itself derived from the fact that the curve describing the shock wave must satisfy at least the following two conditions. First, far from the leading edge of the shock wave, the angle defining the slope of the curve is given by

$$\mu = \sin^{-1}(1/M) \tag{47}$$

Second, at the leading edge, the tangent to the curve is perpendicular to the direction of travel. Although there are a number of curves that satisfy these conditions, the simplest curve that does so is the hyperbola. The specific form of the hyperbola that is appropriate for shock wave characterization is obtained as follows.

Consider the generic two-dimensional hyperbola shown in Fig. 5. We recall the following properties of such a hyperbola in Cartesian coordinates.

Equation:

$$(x/a)^2 - (y/b)^2 = 1 \tag{48a}$$

Asymptote slope:

$$m = b/a \tag{48b}$$

Relationship between c and a:

$$c^2 = a^2 + b^2 \tag{48c}$$

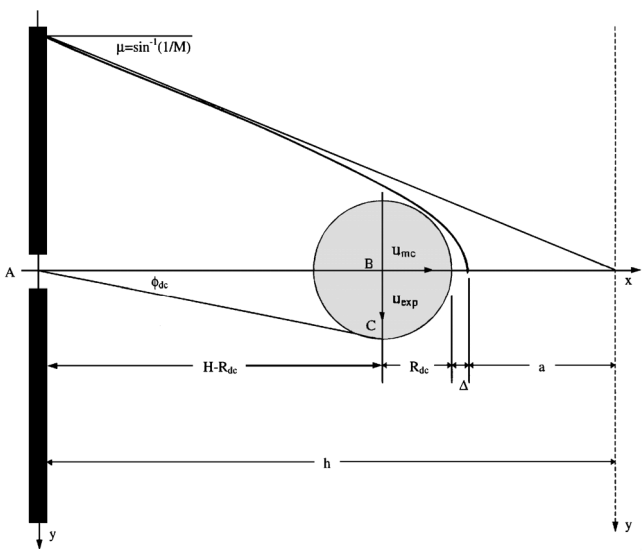

Fig. 5 Two-dimensional hyperbola model for a debris cloud induced shock wave.

where a is the distance from the origin to the vertex and c is the distance from the origin to the focus. Next, we note that Eq. (47) implies that the slope of the curve can also be written as

$$m = 1/\sqrt{M^2 - 1} \tag{49}$$

Equating Eqs. (48b) and (49) allows us to solve for b in terms of a, that is,

$$b = a/\sqrt{M^2 - 1} \tag{50}$$

Finally, as shown in Fig. 5, we place the center of mass of the debris cloud at the focus of the hyperbola. In this case, we note that the leading edge of the shock wave is located at some distance Δ ahead of the debris cloud, which has some characteristic radius R_{dc}. This distance Δ is obtained from elementary shock physics theory[11] and is given by

$$\Delta = 0.8 R_{dc}(\rho_{0a}/\rho_{Ha}) \tag{51}$$

where ρ_{Ha} is given by Eq. (28) and R_{dc} is given by Eqs. (44a) and (44b). Once the center-of-mass of the internal debris cloud is placed at the focus of the hyperbola, it follows that the distance from the origin to the focus can also be written as

$$c = a + \Delta + R_{dc} \tag{52}$$

Substituting for b in terms of a according to Eq. (50) into Eq. (48c), solving for c, equating the result to Eq. (52), and solving for a finally yields

$$a = \frac{\Delta + R_{dc}}{M/\sqrt{M^2 - 1} - 1} \tag{53}$$

Because a and b are now both determined, the equation for the hyperbola approximating the shape of the shock wave created by a moving internal debris cloud is also completely determined. However, to be applicable to the two-dimensional coordinate system shown in Fig. 3, the x coordinate in Eq. (41a) must be offset by an amount h, that is, the equation for the two-dimensional hyperbola is now written as

$$[(x - h)/a]^2 - (y/b)^2 = 1 \tag{54}$$

The quantity h is obtained by noting that the origin in Fig. 5 is shifted over an amount $H + \Delta + a$ when compared to the origin in Fig. 3; hence,

$$h = H + \Delta + a \tag{55}$$

In three dimensions, making use of the axial symmetry about the x axis, Eq. (55) becomes

$$[(x - h)/a]^2 - (y/b)^2 - (z/b)^2 = 1 \tag{56}$$

Thus, the position of the shock wave at the onset of attenuation is now defined, and the various regions of interest already discussed can be readily defined through a series of relatively simple calculations in analytic geometry.

Comparison with Experimental Results

Test Configurations and Impact Parameters

The predictions of the model developed herein are compared against the experimental results obtained from four high-speed impact tests. Table 1 presents a summary of the geometric and impact

Table 1 Impact parameters and system geometries

Test no.	d_p, cm	V_p, km/s	t_b, cm	S, cm	t_w, cm	Inner bumper
1	1.27	6.70	0.16	11.43	0.48	type A
3	1.59	6.42	0.16	11.43	0.48	type A
5	1.59	6.58	0.16	11.43	0.48	type B
6	1.59	6.50	0.16	11.43	0.48	type A

parameters for the four impact tests. Spherical projectiles were used in all of the tests in order to produce relatively uniform primary debris clouds. The MLI in the type A inner bumpers consisted of 20 Mylar® layers. In the case of the type B inner bumper,[12] the multilayer composite material panel consisted of six layers of Nextel® AF62, six layers of Kevlar® 710, and a 0.203-cm-thick graphite/epoxy panel. In all of the tests, the initial ambient temperature behind the pressure wall was 24°C = 297 K.

Experimental results were obtained by pressure and temperature sensors placed at increasing distances behind the pressure wall. These sensors were placed in three pairs symmetrically about the line defining the original impact trajectory. In subsequent discussions they are referred to as (1E, 1W), (2E, 2W), and (3E, 3W); sensors 1W, 2W, and 3W were the mirror images of sensors 1E, 2E, and 3E, respectively. The straight line distances from the impact point on the inner wall to the three pairs of sensors were 64, 134, and 212 cm, respectively, with sensor pair (1E, 1W) being the closest and (3E, 3W) being the farthest. Figure 6 presents a sketch showing the locations of the various sensors.[13]

Model Parameter Values

As discussed in the preceding sections, the results produced by the analytical model depend on the values of the empirical constants n and C_D. Poorly chosen values could lead to either spurious results (e.g., negative or imaginary debris cloud expansion velocities) or unrealistic results (e.g., debris clouds that area either too heavy or too light). In addition, an improper internal debris cloud drag coefficient value could result in debris clouds that stop either too soon or too late. Naturally, a fairly substantial experimental database is required to determine specific values of the empirical constants and the drag coefficient as functions of projectile diameter, impact velocity, system geometry, etc.

In the absence of such an extensive database, two series of trial runs were performed. The objective of the first was to gain insight into the effects of the various constants on the predictions of the analytical model. The objective of the second was to determine preliminary values of the constants n and C_D for use in the initial comparisons between the predictions of the model with experimental results. Table 2 presents a summary of the final values for the empirical constants n and C_D as a function of inner bumper type (A or B) and projectile diameter d_p that were obtained from these exercises. The use of the constant m shown in Table 2 is discussed in a later section.

Table 2 Initial empirical constant values

Empirical constant	Type A inner bumper d_p, cm		Type B inner bumper d_p, cm
	1.27	1.59	1.59
n	0.50	2.50	1.10
C_D	0.20	0.30	0.11
m	0.60	0.70	1.25

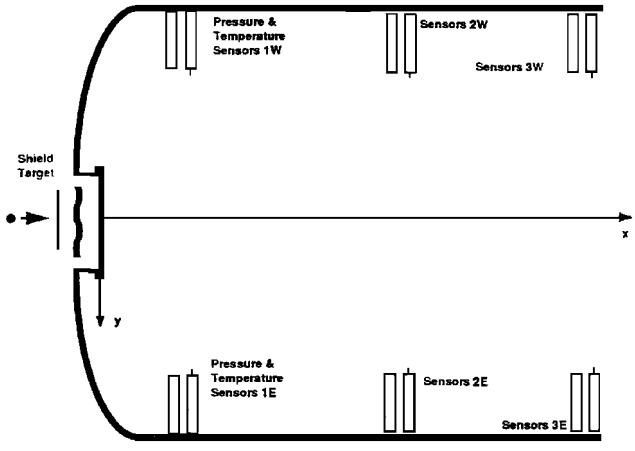

Fig. 6 Sensor arrangement and typical test setup.[13]

Comparison of Model Predictions with Experimental Results

Using the empirical constants in Table 2, model predictions were obtained for the test conditions listed in Table 1. A comparison of the experimental results and the predictions of the model developed herein revealed that the model performed reasonably well in predicting the pressures experienced by sensors 1E, W. However, with regard to the other sensors, although the model correctly predicted substantial pressure decreases at sensors 2E, W and 3E, W, the predicted values were significantly lower than the experimental values. It was as if the attenuation of the peak pressures occurred too rapidly with distance away from the shock wave. Based on the significant differences observed between the predictions of the analytical model and the experimental results at sensors 2E, W and 3E, W, it was apparent that some adjustment of the analytical model was needed.

Internal Effects Model Modifications

To lessen the rapidity with which the model predicts the attenuation of the peak pressures and temperatures, it is proposed that Eq. (32), which calculates distance using a nondimensional position quantity, be modified by introducing an empirical constant to control the rate of attenuation as follows:

$$\eta = \kappa_2 R'(E/P_{0a})^{\frac{1}{3}} \tag{57}$$

where $\kappa_2 > 1$. Choosing a value of $\kappa_2 > 1$ would serve to stretch out the attenuation process so that at points far from the shock wave, the pressures are not quite as low as they would be without the empirical factor. The following expression for κ_2 appears to capture this desired feature:

$$\kappa_2 = \begin{cases} 1, & x_{\text{poi}} \le H \\ 1 + m(100R')^m, & x_{\text{poi}} > H \end{cases} \tag{58}$$

This form is motivated by the desire to include stretching effects in the attenuation of peak pressures and temperatures only for points of interest that are relatively far removed from the shock wave or the internal debris cloud. Points of interest relatively near the shock wave or debris cloud experience normally attenuated pressure and temperature magnitudes.

Following the modification of the analytical model, a value of m was determined that would extend the effects of the shock wave induced pressure and temperature increases farther away from the shock wave and the debris cloud. In doing so, the empirical constant n and the drag coefficient C_D were kept at the values shown in Table 2. The final values of the constant m are presented in the last row of Table 2. The constants in Table 2 will likely yield acceptable results only for the system geometries, projectile diameters, and impact velocities considered in the experimental phase of this effort. Although the analytical model will certainly produce results for other system geometries, projectile diameters, and impact velocities, those results may not be appropriate for the alternative parameters considered.

Comparison of Modified Model Predictions with Experimental Results

Table 3 presents a comparison of the experimental results and the predictions of the model developed herein using the empirical constants given in Table 2. As can be seen in Table 3, the predictions of the model compare favorably with the experimental results. The most significant difference between the experimental results and the model predictions is found for the temperature increases for test 3. Interestingly enough, the corresponding pressure increase values predicted by the model for this test do agree rather well with the experimental results. A comparison of the test conditions, etc., for tests 3 and 6 reveals that the two are virtually identical; the only difference is that the velocity for test 6 was 0.8 km/s higher than that for test 3. Inspection of the experimental results for these two tests shows that the pressure increases sustained during the two tests are, in fact, very similar. However, with the exception of sensors 3E,W, the temperature increases are quite different: those recorded in test 6 are substantially lower than those in test 3. Because the analytical model predictions agree well with the pressure readings in both tests,

Table 3 Pressure and temperature prediction comparisons

	Pressure increase		Temperature increase	
Sensor	Experimental result, ψ	Model prediction, ψ	Experimental result, °C	Model prediction, °C
		Test 1		
1E	17	15.2	18	43.2
1W	18	15.2	27	43.2
2E	4	7.2	23	23.0
2W	6	7.2	20	23.0
3E	3	3.2	25	11.6
3W	2	3.2	n/a	11.6
		Test 3		
1E	21	24.3	104	63.9
1W	21	24.3	118	63.9
2E	17	17.2	139	46.6
2W	21	17.2	94	46.6
3E	8	8.0	n/a	25.1
3W	8	8.0	40	39.0
		Test 5		
1E	34	34.2	64	82.7
1W	40	34.2	54	82.7
2E	10	10.2	34	30.0
2W	15	10.2	31	30.0
3E	3	5.6	n/a	18.2
3W	4	5.6	n/a	21.5
		Test 6		
1E	16	24.6	20	64.8
1W	31	24.6	65	64.8
2E	15	17.8	52	48.1
2W	14	17.8	63	48.1
3E	12	8.3	44	25.8
3W	7	8.3	n/a	40.1

as well as the temperature readings in test 6, the inference to be drawn is that the temperature readings in test 3 must be due to some phenomenon not included in the analytical model developed herein.

Conclusions and Recommendations

A first-principles-based model has been developed to predict the effects of a perforating orbital debris particle impact within a pressurized habitable module. The model was developed in a way such that it sequentially characterizes the phenomena associated with the impact event, including the initial impact on the outer bumper, the creation and motion of the debris clouds within the module wall system, the impact of the debris clouds on the module pressure wall, the creation and motion of the debris cloud that enters the module interior, and the effects of the debris cloud within the module on pressure and temperature levels.

The model development has been accomplished through the application of elementary shock physics and thermodynamic theory, as well as the principles of mass, momentum, and energy conservation. The predictions of the model were compared against experimental results obtained from four high-speed impact tests. Several modifications were made to the basic model to bring its predictions closer in line with the experimental results, including decreasing the rapidity with which the model predicts the attenuation of peak pressures and accompanying temperature increases. Following the adjustment of several empirical constants, the predictions of the modified internal effects model were in much closer agreement with the experimental results.

Following a review of the methodology used to develop the internal effects model presented herein, the following recommendations are offered as suggestions for improving the robustness of the model, as well as for improving its ability to model the phenomena associated with the high-speed impact of a pressurized module. First, the effects of backsplash due to impact of the projectile on the outer bumper should be included in the analytical model. This would have the effect of decreasing the mass of the primary debris cloud, but, due to momentum conservation, increasing its center-of-mass velocity (the so-called momentum enhancement effect). Because the energy of the debris cloud is proportional to the square of the velocity, this could have a significant impact on the subsequent effects produced by the primary debris cloud. In addition, including the effects of light flash in the energy balance for the initial impact on the outer bumper would also have the effect of producing more accurate primary debris cloud velocities.

Second, inner bumper burning and/or melting may be a significant energy absorbing mechanism and may have a significant influence on the energy balance that is applied to the system before and after the impact of the primary debris cloud on the inner bumper. Hence, it should be included in the analytical model development.

Third, the analytical model should include the effects of pressure wall deformation, including hole formation, bulging, cracking, etc. This would affect the amount of energy that is available for the motion of the internal debris cloud and the creation of the accompanying shock waves within the module interior.

Fourth, the shock wave attenuation scheme for the internal debris cloud could be improved by adjusting the present model to include an internal debris cloud whose speed decays as it moves into the module interior as opposed to ceasing motion in a rather abrupt manner.

Finally, the analytical model should be expanded to oblique impacts and nonspherical projectiles. This would render the model applicable to a much wider variety of impact scenarios. In addition, additional internal effects testing at different velocities using alternative system geometries and impact conditions should be performed. This would provide additional information that would facilitate the implementation of the recommendations presented herein as well as validate the model for a much larger family of impact events.

Acknowledgments

The authors would like to acknowledge the support of the NASA Marshall Space Flight Center under Contract NCC8-28. J. D. Johnson at the Los Alamos National Laboratory provided valuable assistance in obtaining the equation-of-state for air. The authors are also grateful to Werner Dahm, NASA Marshall Space Flight Center; Michael Krause, Redstone Technology Test Center; and Gary Hough, University of Alabama in Huntsville Aerophysics Research Center, for their many helpful comments during this effort.

References

[1]Gehring, J. W., Lathrop, B. L., and Warnica, R. L., "Spacecraft Interior Hazards from Hypervelocity Impact," GM Defense Research Lab., TR-66-13, Santa Barbara, CA, March 1966.

[2]Long, L. L., and Hammitt, R. L., "Meteoroid Perforation Effects on Space Cabin Design," AIAA Paper 69-365, April 1969.

[3]Engler, E. E., "Physiological and Safety Aspects of Penetration," *Space Debris and Meteoroid Technology Workshop*, NASA Marshall Space Flight Center, Huntsville, AL, Sept. 1984.

[4]Weibull, G. W., "A Proposal for Blast Incapacitation Criteria Concerning Soldiers Inside Armored Vehicles," *Proceedings of the 9th International Symposium on Ballistics*, Royal Military College of Science, England, UK, 1986, pp. 2-337–2-344.

[5]Rice, M. H., McQueen, R. G., and Walsh, J. M., "Compression of Solids by Strong Shock Waves," *Solid State Physics*, Vol. 6, edited by F. Seitz and D. Turnbull, Academic, New York, 1958, pp. 1–63.

[6]Anderson, C. E., Trucano, T. G., and Mullin, S. A., "Debris Cloud Dynamics," *International Journal of Impact Engineering*, Vol. 9, No. 1, 1990, pp. 89–113.

[7]Jolly, W. H., "Analytical Prediction of Hole Size Due to Hypervelocity Impact of Spherical Projectiles," M.S. Thesis, Civil and Environmental Engineering Dept., Univ. of Alabama, Huntsville, AL, Dec. 1993.

[8]Maiden, C. J., Gehring, J. W., and McMillan, A. R., "Investigation of Fundamental Mechanism of Damage to Thin Targets by Hypervelocity Projectiles," General Motors Defense Research Lab., TR-63-225, Santa Barbara, CA, Sept. 1963.

[9]Rinehart, J. S., "Stress Transients in Solids," HyperDynamics, Santa Fe, NM, 1975.

[10]Baker, W., *Explosions in Air*, Texas Univ. Press, Austin, TX, 1973.

[11]Hayes, W. D., and Probstein, R. F., *Hypersonic Flow Theory*, Academic, New York, 1966.

[12]Christiansen, E. L., "Design and Performance Equations for Advanced Meteoroid and Debris Shields," *International Journal of Impact Engineering*, Vol. 14, Nos. 1–4, 1993, pp. 145–156.

[13]Williamsen, J. E., and Serrano, J., "Atmospheric Effects in Spacecraft Interiors Following Orbital Debris Penetration," *Proceedings of the SPIE Symposium on Space Environmental, Legal, and Safety Issues* (Orlando, FL), SPIE, Bellingham, WA, 1995, pp. 40–51 (Paper 2483-06).

A. C. Tribble
Associate Editor